Chapter 9
Ion Induction Accelerators

John J. Barnard and Kazuhiko Horioka

The description of beams in RF and induction accelerators share many common features. Likewise, there is considerable commonality between electron induction accelerators (see Chap. 7) and ion induction accelerators. However, in contrast to electron induction accelerators, there are fewer ion induction accelerators that have been operated as application-driven user facilities. Ion induction accelerators are envisioned for applications (see Chap. 10) such as Heavy Ion Fusion (HIF), High Energy Density Physics (HEDP), and spallation neutron sources. Most ion induction accelerators constructed to date have been limited scale facilities built for feasibility studies for HIF and HEDP where a large numbers of ions are required on target in short pulses. Because ions are typically non-relativistic or weakly relativistic in much of the machine, space-charge effects can be of crucial importance. This contrasts the situation with electron machines, which are usually strongly relativistic leading to weaker transverse space-charge effects and simplified longitudinal dynamics. Similarly, the bunch structure of ion induction accelerators relative to RF machines results in significant differences in the longitudinal physics.

In this chapter, ion sources and injectors are covered in Sect. 9.1. Ion sources have different practical issues than electron sources (see Sect. 7.2). Longitudinal dynamics are covered in Sect. 9.2 while emphasizing strong space-charge issues specific to ion induction accelerator applications. The physics of transverse dynamics with strong space-charge forces is left to references [42], [1], and [2], for example.

9.1 Ion Sources and Injectors

Induction ion accelerator applications with high space-charge intensity need high perveance beam sources in pulses that typically range from $\sim$10 ns to $\sim$10 μs. Compared with electron beam generation, ions are more difficult to extract from the source. The generation, extraction, and propagation of the ions are strongly influenced by both longitudinal and transverse space-charge effects and plasma

J.J. Barnard (✉)
Lawrence Livermore National Laboratory, Livermore, CA 94550, USA
e-mail: jjbarnard@llnl.gov

K. Takayama, R.J. Briggs (eds.), *Induction Accelerators*, Particle Acceleration and Detection, DOI 10.1007/978-3-642-13917-8_9,

phenomena. Currents of high-power ion beam sources are limited by the gap structure and the properties of the ion source. Important properties include the available ion current-density, the ion species and purity (including their charge state), and the stability of the emitting surface. We first review basic physical concepts required for understanding the gap dynamics (Sect. 9.1.1), including: space-charge limited flow (Child-Langmuir emission), plasma limited flow (Bohm criterion) and the ion emitting surface in plasmas, transverse and longitudinal beam emittance, electrode geometry, transients in the diode, and longitudinal accelerative cooling. Then we review specific ion sources presently employed or showing promise for high current induction accelerators (Sect. 9.1.2) and finally review several complete injector systems (Sect. 9.1.3).

9.1.1 Physics of High Current-Density Ion Sources

Options for ion sources depend on the available ion current-density and beam transport limitations associated with the injector geometry. To evaluate options, we need to know the relationship between plasma parameters, the space-charge field, and the attainable ion current-density.

1D Child-Langmuir extraction: In low energy transport, particularly within the beam extraction section (diode), the charged particle motion is dominated by the space-charge field. We estimate [1, 2] the steady-state (mid-pulse) current produced of a species-pure ion beam when there is a voltage of magnitude V applied across a gap of distance d, as illustrated in Fig. 9.1. The flow is assumed to be independent of transverse radius and varies only with longitudinal position z in the gap. The source can represent any pure species ion emitter which can produce adequate current-density. In steady state, the continuity equation implies that the axial current-density $J_z = \rho v_z$ is constant as a function of z, where ρ is the charge-density of the beam and v_z is the axial particle velocity in the gap. The one-dimensional Poisson equation $\partial^2\phi/\partial z^2 = -\rho/\epsilon_0$ governs the relation between the electrostatic potential ϕ and the charge-density ρ. The velocity is related to ϕ by the steady-state (non-relativistic) momentum equation $mv_z\partial v_z/\partial z = -q\,\partial\phi/\partial z$ yielding the energy

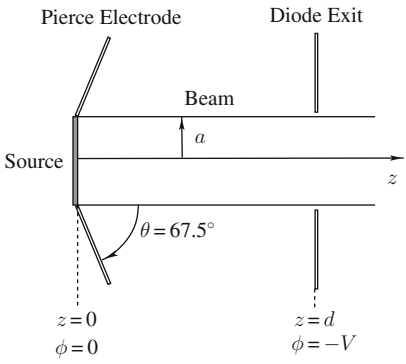

Fig. 9.1 Diode geometry

conservation equation $(1/2)mv_z^2 = -q\phi$. Here we have assumed zero pressure (cold beam) in the momentum equation. For convenience, the potential ϕ is chosen to be zero at the emitter and $-V$ at the diode exit. The charge-density ρ in the Poisson equation can thus be expressed in terms of ϕ yielding the differential equation:

$$\frac{\mathrm{d}^2\Phi}{\mathrm{d}z^2} = \frac{J_z}{\epsilon_0 v_z} = \frac{J_z}{\epsilon_0}\left(\frac{m}{2q\Phi}\right)^{1/2}. \tag{9.1}$$

Here we have denoted $\Phi \equiv -\phi$ for the sake of clarity to minimize negative signs in the derivation. We multiply Eq. (9.1) by $\mathrm{d}\Phi/\mathrm{d}z$ and integrate to obtain:

$$\frac{1}{2}\left(\frac{\mathrm{d}\Phi}{\mathrm{d}z}\right)^2 = \frac{J_z}{\epsilon_0}\left(\frac{2m}{q}\right)^{1/2}\Phi^{1/2} + C \tag{9.2}$$

Here, C is an integration constant. We further assume that space-charge is plentiful enough that it may be extracted from the emitting surface (or from a plasma source) at $z = 0$ such that the longitudinal field $E_z = \partial\phi/\partial z$ is reduced to zero right at the surface. This is the so-called "space-charge limited emission" condition. If more space-charge were extracted, it would create an electric field that would be directed towards the emitter and thus prevent further emission. The steady-state condition occurs when $\partial\Phi/\partial z = 0$ is maintained at the emitter. This condition (together with the condition that $\Phi = 0$ at $z = 0$) requires $C = 0$ in Eq. (9.2). Taking the square root of Eq. (9.2) and solving the resulting differential equation (again subject to $\Phi = 0$ at $z = 0$), yields

$$\Phi(z) = \frac{3^{4/3}}{2^{5/3}}\left(\frac{J_z}{\epsilon_0}\right)^{2/3}\left(\frac{m}{q}\right)^{1/3} z^{4/3}. \tag{9.3}$$

Setting $\Phi = V$ at $z = d$, gives $\Phi = V(z/d)^{4/3}$ and so V satisfies,

$$V = \frac{3^{4/3}}{2^{5/3}}\left(\frac{J_z}{\epsilon_0}\right)^{2/3}\left(\frac{m}{q}\right)^{1/3} d^{4/3}. \tag{9.4}$$

Solving for the current-density J_z yields the so-called Child-Langmuir Law for the current-density of space-charge limited emission:

$$J_z = J_{\mathrm{CL}} \equiv \chi\frac{V^{\frac{3}{2}}}{d^2}, \tag{9.5}$$

where

$$\chi = \frac{4\epsilon_0}{9}\sqrt{\frac{2q}{m}}. \tag{9.6}$$

In addition to the space-charge effect, voltage breakdown limits the value of V used for beam extraction. Empirically it has been found that [3] for small gap distances (for $d \lesssim 1$ cm) there is an electric field maximum of around 100 kV/cm that gives a reasonable design upper limit to avoid electrical breakdown across the gap. In this regime, the maximum voltage $V = V_{\rm BD}$ corresponding to this limit therefore scales with d as $V_{\rm BD} \simeq 100$ kV $(d/1$ cm). For gap distances larger than $d = 1$ cm however, a smaller electric field is required to prevent breakdown, and in this case the design limit scales as $V_{\rm BD} \simeq 100$ kV$(d/1$ cm$)^{1/2}$. Substituting these relations into Eq. (9.5) gives

$$J_z \propto \frac{V^{3/2}}{d^2} \propto \begin{cases} d^{-1/2} & d \lesssim 1 \text{ cm}, \\ d^{-5/4} & d \gtrsim 1 \text{ cm}. \end{cases} \tag{9.7}$$

Therefore, the current-density decreases as the gap length increases in operation close to the breakdown limit.

For a circular beam with constant radius a within the gap, the extractable total ion current I is given by,

$$I = \pi a^2 J_{\rm CL} = \pi \chi \left(\frac{a}{d}\right)^2 V^{\frac{3}{2}}. \tag{9.8}$$

The radius of the diode aperture is typically slightly larger than the beam radius a. If a is too large compared with the gap width d, the equi-potential lines will be distorted and the negative lens effect [4] can become large. Pierce electrodes (see Fig. 9.1 and the subsection below) are employed to shape the field and maintain approximate 1D flow. Even with Pierce electrodes, to avoid beam aberrations, the aspect ratio of the extraction gap a/d is typically limited to $a/d < 0.25$ [5]. This scaling implies that for a fixed aspect ratio, the maximum extractable beam current depends only on the extraction voltage as $I \propto V^{\frac{3}{2}}$. Note that these scaling relations imply that when producing high current using a single beam, the current-density decreases as the beam current increases.

Transverse beam emittance: The ion temperature at the source, together with radius of the source determine the initial transverse phase-space area, or equivalently the emittance, of the beam. We assume a uniform current-density at the source so that $\langle x^2 \rangle_\perp = a^2/4$ and we also assume a nonrelativistic Maxwell Boltzmann distribution in the spread of particle angles, so that $\frac{1}{2} m v_z^2 \langle x'^2 \rangle_\perp = k_B T_i/2$, where $\langle \cdots \rangle_\perp$ denotes an average over the transverse phases space (x, x', y, y'). Here, a and T_i are the beam radius and ion temperature at the source, respectively, and k_B is Boltzmann's constant. Both of the assumptions above are good near the emitting surface. If there is no angular divergence in a, then $a' = 4\langle x x' \rangle_\perp / a = 0$, and the initial normalized emittance $\varepsilon_{nx} = 4\gamma_b \beta_b [\langle x^2 \rangle_\perp \langle x'^2 \rangle_\perp - \langle x x' \rangle_\perp^2]^{1/2}$ (see [1]) at the source is

$$\varepsilon_{nx} = 4 \left\langle x^2 \right\rangle_\perp^{1/2} \left\langle \frac{v_x^2}{c^2} \right\rangle_\perp^{1/2} = 2a \left(\frac{k_B T_i}{mc^2}\right)^{1/2}. \tag{9.9}$$

Here, $v_x = \mathrm{d}x/\mathrm{d}t \simeq \beta_b c x' = v_z x'$ has been applied in the nonrelativistic limit with $\gamma_b = 1$. Assuming conservation of normalized emittance, then the unnormalized emittance $\varepsilon_x = c\varepsilon_{nx}/v_z$ exiting the diode can be expressed as,

$$\varepsilon_x = 2a\left(\frac{k_B T_i}{m v_z^2}\right)^{1/2} = \sqrt{2}a\left(\frac{k_B T_i}{qV}\right)^{1/2}, \tag{9.10}$$

where $qV = \frac{1}{2}mv_z^2$ is the ion kinetic energy at the diode exit. Beam optical aberrations (non-linear transverse electric fields) will increase the emittance from the initial source value given by Eq. (9.10). Electrodes near the edge of the beam are used to shape the electric field so that nearly parallel flow can be maintained (see Pierce electrodes subsection below) and aberrations minimized. However, because the electrodes cannot be made to be ideal, diode normalized emittance can be significantly higher than Eq. (9.9).

Longitudinal beam emittance and accelerative cooling: Analogously to the transverse case the longitudinal phase-space area in our ideal 1D diode is also conserved. Here the appropriate phase-space variables are those that form conjugate pairs, such as the longitudinal energy $\mathcal{E}_z \equiv p_z^2/2m$ and arrival time t, or the longitudinal momentum p_z and the longitudinal position z. At the source there is a spread in longitudinal energy corresponding to the temperature at the source, such that $\langle \delta p_z^2 \rangle/(2m) = k_B T_i/2$. Here, $\langle \cdots \rangle$ denotes an average over the 6D distribution function, and δp_z and $\delta \mathcal{E}_z$ are the difference between the longitudinal momentum and energy of a particle and their respective means. After passing through an ideal diode, all particles receive the same energy increment qV so the spread in longitudinal energy remains the same as it is at the source. For a pulse duration at the source τ_p, the duration at the exit will also be τ_p, so the longitudinal (normalized) emittance that is proportional to $\langle \delta \mathcal{E}_z^2 \rangle^{1/2} \tau_p$ will be conserved as expected. But the consequence of having a conserved normalized emittance implies that the temperature of the beam (as measured in the co-moving frame) is drastically reduced.

To calculate the energy spread in the co-moving frame, it is most convenient to first calculate δv_z for a particle in the laboratory frame. For a non-relativistic boost, velocities are additive, so the velocity difference δv_z and momentum difference δp_z in the co-moving frame are the same as those quantities in the lab frame. Since $\mathcal{E}_z = p_z^2/2m$, it follows that $\delta \mathcal{E}_z = p_z \delta p_z/m$, or $\delta \mathcal{E}_z/\mathcal{E}_z = 2\delta p_z/p_z$. If we denote subscript "source" and "exit" for quantities at the diode source and exit respectively, then the longitudinal temperature in the co-moving frame $k_B T_{z,\mathrm{exit}}$ is given by:

$$\frac{k_B T_{z,\mathrm{exit}}}{2} = \frac{\langle \delta p_{z,\mathrm{exit}}^2 \rangle}{2m} = \frac{\langle \delta \mathcal{E}_{z,\mathrm{exit}}^2 \rangle}{4\mathcal{E}_{z,\mathrm{exit}}} = \frac{\langle \delta \mathcal{E}_{z,\mathrm{source}}^2 \rangle}{4\mathcal{E}_{z,\mathrm{exit}}} = \frac{3}{16}\frac{(k_B T_{\mathrm{source}})^2}{\mathcal{E}_{z,\mathrm{exit}}} \tag{9.11}$$

Here, the final equality uses the result that, for a Maxwell-Boltzmann distribution, the average $\langle \delta \mathcal{E}_z^2 \rangle = 3(k_B T)^2/4$. As can be seen from Eq. (9.11) the longitudinal

temperature of the beam $k_B T_{z,\mathrm{exit}}$ has decreased by a factor of order $k_B T_{\mathrm{source}}/\mathcal{E}_{z,\mathrm{exit}}$. For $k_B T_{\mathrm{source}} \sim 0.1$ eV, and $\mathcal{E}_{z,\mathrm{exit}} \sim 10^5$ eV, the temperature has decreased by a factor of order 10^{-6}. This large reduction in temperature can be seen as a result of the effective lengthening of the beam. Since the initial longitudinal length of the beam is of order $\delta p_{z,\mathrm{source}} \tau_p / m$, and the length of the beam at the diode exit is of order $p_{z,\mathrm{exit}} \tau_p / m$, the beam has been stretched by a factor $p_{z,\mathrm{exit}}/\delta p_{z,\mathrm{source}}$ so the momentum spread $\delta p_{z,\mathrm{exit}} = \delta p^2_{z,\mathrm{source}}/p_{z,\mathrm{exit}}$ has gone down by the same factor, implying that the temperature has gone down by a factor $\sim k_B T_{\mathrm{source}}/\mathcal{E}_{z,\mathrm{exit}}$, consistent with Eq. (9.11).

Whereas the length of the beam has gone up by a large factor (with a concomitant decrease in the longitudinal temperature), the transverse dimension of the beam (and transverse temperature) remain nearly constant. The distribution function in the beam frame has thus become highly anisotropic. This can lead to dynamic instabilities [6–8] that saturate when the longitudinal temperature approaches the transverse temperature. Collisions also tend to reduce the magnitude of the anisotropy by transferring momentum from the transverse degrees of freedom into longitudinal momentum spread. This is known as the Boersch effect [1]. Even though collisions are generally negligible in beams, since longitudinal cooling is so extreme, the few collisions that do occur can increase the longitudinal temperature to a value far higher than given by Eq. (9.11).

Plasma sources: the Bohm criterion and ion emission surface: Many high current-density ion sources rely on extraction from a plasma surface. Important phenomena in plasma-based high current-density include: escape of electrons from the emitter, drift of ions toward the plasma surface, acceleration of ions, injector geometry and applied fields, space-charge and plasma effects and associated transport limitations.

When an electric field is applied to the source plasma, the externally applied field is shielded by the plasma sheath. The characteristic distance over which the electric field is excluded is the *Debye length* [9, 10]

$$\lambda_D = \sqrt{\frac{\epsilon_0 k_B T_e}{e^2 n_e}} = 743 \text{ cm} \sqrt{\frac{T_e/(\text{eV})}{n_e/(\text{cm}^{-3})}}. \tag{9.12}$$

Here, $-e$ is the electron charge, and T_e and n_e are the electron temperature and density. Because the ions are extracted from the plasma through the sheath region so long as the dimensions of plasma volume are much larger than λ_D, this is the basic scale length of the plasma source. In plasma ion sources, the boundary between electrically neutral source plasma and the sheath region is called the *ion emission surface*. The ion emission surface, the emitted current, and the geometry and biases of the injector structures will determine the ion optics.

The current of ions extracted is limited by the available ion current-density through the sheath and/or the space-charge field in the extraction gap. When ions are extracted from a stationary plasma, the current-density is limited by the thermal motion of the source plasma. Assuming a Maxwellian velocity distribution in the

source plasma, we can derive the characteristic *Bohm current-density* which gives the available current-density of ions [4]. The Bohm current-density is

$$J_B = 0.6en_i \left(\frac{\kappa T_e}{m_i}\right)^{\frac{1}{2}}, \tag{9.13}$$

where n_i is the plasma ion density and m_i is the ion mass. Equation (9.13) indicates that high current-density sources require higher temperature plasmas. On the other hand, the intrinsic emittance of the beam emerging from the ion source is given by Eq. (9.10).

Because the equilibration time between electrons and ions is usually long enough, the Bohm limit can not be directly related with the intrinsic beam emittance. However these indicate that the relation between the available current-density and the intrinsic beam emittance is a trade-off; increasing the current level means decreasing the quality of extracted beam.

The optics of ions extracted strongly depend on the plasma source. Figure 9.2 shows a schematic of the stationary ion emitting surface in a long-pulse plasma source. Here, we define the "anode" as the ion emitting surface, and the "cathode" as the diode exit. (In general, current flows from anode to cathode.) When the ion supply is sufficient to extract, the current and the beam optics are governed by the self field in the extraction gap. If the Bohm current-density is less than the Child-Langmuir current-density ($J_B < J_{CL}$), then the source is starved and a concave emission surface results which produces an over-focused beam as illustrated in Fig. 9.2(a). Conversely, if $J_B > J_{CL}$, then there is an excess supply of ions resulting in a convex emission surface and produces a divergent beam as illustrated in Fig. 9.2(b). For good beam optics, a slightly starved source is considered preferable. This guiding principle limits the aspect ratio of the extraction gap [11].

Pierce electrodes: As discussed above, Child-Langmuir flow is based on the assumption of a one-dimensional (longitudinal) geometry. In fact, diodes have finite

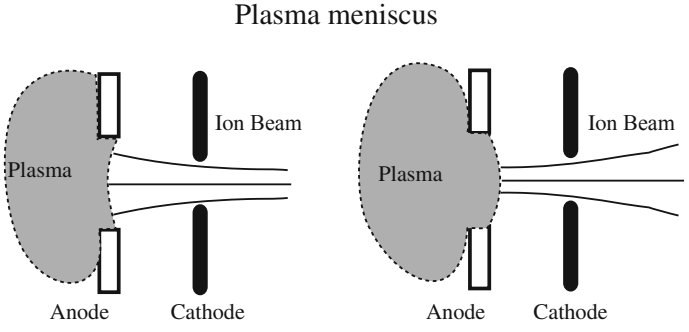

Fig. 9.2 Behavior of the ion emitting surface in extraction from a stationary source plasma for starved (**a**) and excess (**b**) source current-density

transverse extent and so are intrinsically multi-dimensional. Nevertheless, electrodes can be introduced (see Fig. 9.1) that allow the beam to be terminated at a finite radius, yet maintain the same electrical field, velocity, and charge-density, as in the case of a one-dimensional Child-Langmuir flow over the full radial profile of the beam. This can be easily seen in the case of a ribbon beam that propagates in the z direction and is infinite in the y-direction but has some finite width in the x-direction. We take $x = 0$ to be one of the edges of the beam (with $x > 0$ vacuum). We wish to calculate surfaces of equipotentials, such that the potential satisfies the Child-Langmuir potential [$\Phi(x = 0, y, z) = V(z/d)^{4/3}$] and also maintains the 1D condition that the transverse electric field is zero $\partial\phi(x = 0, y, z)/\partial x = 0$ along the edge of the beam. A solution that satisfies both conditions can be found using complex variables. Let $w = z + ix$. Then let $\Phi(x, z)$ be the real part of a complex function $F(w) \equiv \Phi(x, z) + i\mu(x, z)$. If $F(w)$ is an analytic function (i.e. its derivative exists and is independent of direction over some domain in the w plane), then Φ and μ satisfy the Laplace equation over that domain. This suggests that we take $F(w) = V(w/d)^{4/3}$ so that along the surface $x = 0$, $\Phi(x = 0, z) = V(z/d)^{4/3}$ implying that $\Phi(z)$ satisfies the Child-Langmuir potential. The real part of $F(w)$ can be written:

$$\mathrm{Re}[F(w)] = \Phi(x, z) = V(x^2 + z^2)^{2/3} \cos\left[\frac{4}{3}\tan^{-1}\left(\frac{x}{z}\right)\right] \tag{9.14}$$

Note that $\Phi(x, z) = \Phi(-x, z)$ so that $\partial\Phi/\partial x|_{x=0} = 0$, as required.

If the source ($z = 0$) is at the equipotential $\Phi = 0$, then the equipotential surface that originates at $x = 0$ and $z = 0$ can be shown from Eq. (9.14) to satisfy $0 = \cos[4\tan^{-1}(x/z)/3]$ implying that $\tan^{-1}(x/z) = 3\pi/8 \simeq 67.5°$. The coordinates of the equipotential passing through $x = 0$ and $z = z_0$ satisfies:

$$z_0^{4/3} = (x^2 + z^2)^{2/3} \cos\left[\frac{4}{3}\tan^{-1}\left(\frac{x}{z}\right)\right] \tag{9.15}$$

By placing conductors along these equipotentials the Child-Langmuir potential is enforced along the edge and therefore throughout the beam. In particular at $z = 0$ an electrode placed at approximately 67.5° from the z-axis is known as a Pierce electrode, and is intended to ensure an initial parallel flow from the source. Electrodes may be placed at larger z along curves given by Eq. (9.15) such as at the diode exit, so that Φ satisfies Eq. (9.14) between electrodes, and therefore ensures Child-Langmuir potential along the beam boundary.

For the case of an axisymmetric cylindrical beam (in contrast to a ribbon beam), there is no simple analytic solution such as Eq. (9.15), but numerical results indicate that at $z = 0$ the same "Pierce angle" of 67.5° is obtained. However, for finite z_0 the curves are different, but qualitatively similar, and instead of lying on surfaces that are independent of y the surfaces are independent of azimuth θ in the axisymmetric case [12].

As discussed above, despite the use of electrodes at, for example, the diode emitter and diode exit, if the diameter of the aperture a is too large compared with the

gap width d, the equi-potential lines will be distorted [4]. This is due to the finite thickness and radius of curvature of conductors that are needed to avoid breakdown, and because fields arising because of departures from the ideal Child-Langmuir geometry can leak in from beyond the exit of the diode.

Diode transients: We saw in the previous section that adding angled electrodes at the edge of the beam compensates for the absence of space-charge beyond the radius of the beam, and thus ensures that the electric field in the location where there is charge-density obeys Child-Langmuir flow. Similarly, during the initial transit of the beam head through the diode, the lack of space-charge in front of the head requires compensation to avoid the effects of the vacuum electric field that occurs between the head of the beam and the exit of the diode. In this case, the compensation is in the form of a time dependent voltage waveform, that is adjusted so that during the initial transit of the head of the beam, the electric field at the head is the same as if there were Child-Langmuir flow. The effect of space-charge between any point in the diode and the diode exit is to reduce the field relative to what it would be if the diode were at the same voltage, but had no space-charge. Therefore, the required waveform will increase with time until the head of the beam reaches the diode exit at which time the potential drop across the diode $\Phi(d)$ will reach the full voltage V for steady Child-Langmuir flow.

We may calculate the required waveform as follows [13]. Suppose the head of the beam is at position z_0 [see Fig. 9.3(a)], with constant current-density J_z at all points between $z = 0$ and $z = z_0$ but $J_z = 0$ between z_0 and the position of the diode exit ($z = d$). If the desired steady-state voltage is V, the potential difference between 0 and z_0 is just the Child-Langmuir potential Φ to the point z_0, $\Phi = V(z_0/d)^{4/3}$. The desired electric field at z_0 is the Child-Langmuir electric field at that point, so $-\partial\phi/\partial z = \partial\Phi/\partial z = (4/3)(V/d)(z_0/d)^{1/3}$. The potential difference between the beam head and the diode exit is $d - z_0$ times this electric field. Summing the potential drops between 0 and z_0 and between z_0 and d yields the desired potential drop across the gap $\Phi(d, z_0)$. Here, we have added a second argument on Φ to indicate that the potential $\Phi(d)$ is calculated when the beam head is at axial position $z = z_0$. We obtain:

$$\begin{aligned}\Phi(d, z_0) &= V\left(\frac{z_0}{d}\right)^{4/3} + \left(\frac{4V}{3d}\right)\left(\frac{z_0}{d}\right)^{1/3}(d - z_0) \\ &= V\left[\frac{4}{3}\left(\frac{z_0}{d}\right)^{1/3} - \frac{1}{3}\left(\frac{z_0}{d}\right)^{4/3}\right]\end{aligned} \tag{9.16}$$

The location of the beam head (z_0) as a function of time can be found by solving the Child-Langmuir energy equation, which can be viewed as a differential equation relating the longitudinal velocity of a particle to the Child-Langmuir potential,

$$\frac{1}{2}m\left(\frac{\mathrm{d}z_0}{\mathrm{d}t}\right)^2 = qV\left(\frac{z_0}{d}\right)^{4/3}. \tag{9.17}$$

The solution to Eq. (9.17), subject to the initial condition $z_0 = 0$ at $t = 0$, is $z_0 = d(t/\tau)^3$, where $\tau = 3d[m/(2qV)]^{1/2}$ is the "transit time" for a particle undergoing

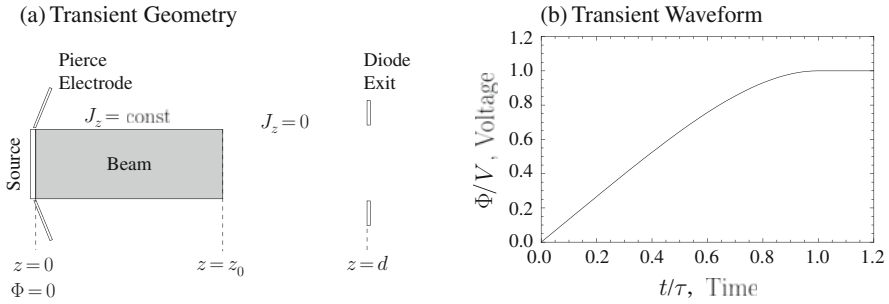

Fig. 9.3 Geometry for transient beam-head calculation (**a**) and the required voltage waveform for an ideal, sharp beam-head (**b**)

Child-Langmuir flow to traverse the diode. Expressing the potential $\Phi(d, z_0)$ in Eq. (9.16) in terms of t instead of z_0 yields

$$\Phi(d,t) = \begin{cases} V\left[\frac{4}{3}\left(\frac{t}{\tau}\right) - \frac{1}{3}\left(\frac{t}{\tau}\right)^4\right], & 0 < t < \tau, \\ V, & t \geq \tau. \end{cases} \tag{9.18}$$

Equation (9.18) specifies how the applied voltage should ramp in time and is plotted in Fig. 9.3(b). Typically this ramping is achieved approximately by raising Φ from 0 to V in a time τ in order to keep the current-density constant during the start up of the diode. If the voltage is turned on with a rise time longer or shorter than this characteristic time τ, beam current oscillations will occur. Such oscillations can have negative consequences since a mismatched beam can strike the aperture, producing secondary particle emission, etc. A similar calculation for the transit of the tail of the beam through the gap yields a rising voltage at the end of the pulse. In this case, a third electrode is needed to cut off the current flow, in the presence of the rising voltage, by allowing the local bias near the source to turn off the space-charge limited emission.

9.1.2 Ion Sources

A large number of ion emitters exist [14] with differing characteristics concerning current-density capability, species purity, transverse emittance, momentum spread and transverse phase-space distortions. In this section we briefly survey features of several technologies and provide references where more details can be found. Electron sources are discussed in Sect. 7.2 and have very different technological issues than ion sources.

Hot-plate sources: A conventional method for extracting metallic ions with low emittance but modest current-density is to use a shaped solid plate as the source. An advantage of plate ion sources is the high degree of control of the shape of the emitting surface, which is a well defined solid boundary which is stable over the

pulse and can be shaped to minimize aberrations. The emitting surface is precisely defined over a wide area with the shaped geometry of the source material. A 17 cm diameter alumino-silicate source was developed and it produced 0.8 A of 1.8 MeV K^+ ions with emittance $\varepsilon < 1.0$ mm-mrad [15, 5, 16]. Various types of material have been employed for hot-plate sources. Alumino-silicates are commonly coated onto tungsten substrates and used for injection of alkali metal ions (Li^+, K^+, Na^+, and Cs^+). Alumino-silicates have a crystal structure with long tunnels, so that alkali ions may flow freely within (even though the material is not a conductor of electrons). The work function to remove these alkali metals (as singly charged ions) from the alumino-silicate is small, so the temperature of the hot-plate need only be raised to ~ 0.1 eV $=$ 1,000°C (in contrast to plasma sources in which $k_B T_i \sim 1$ eV) to produce significant quantities of singly charged ions. The low temperature gives rise to a lower intrinsic emittance. Alumino-silicates are thermionic emitters, with the emission satisfying the Richardson-Dushman equation [17], which states that the current-density is proportional to $T_i^2 \exp(-q\phi_w / k_B T_i)$, where ϕ_w is the effective work function of the material. Thermionic emitters are chosen to have low ϕ_w.

In addition to thermionic emitters (such as alumino-silicates), so-called "contact ionization" sources are also employed as hot-plate sources. These are typically refractory metals, such as tungsten or porous tungsten, that are doped with a surface layer of an alkali carbonate. These emitters have high work functions that exceed the ionization potential of the metallic atoms in the alkali carbonates so when the alkali metal is thermally desorbed there is a high probability it will be desorbed as an ion. If the alkalis are not continuously replenished by feeding material onto either the front or rear surface of the tungsten, the doped tungsten sources will tend to deplete and have smaller lifetimes than the alumino-silicate sources. This follows because the amount of alkali metal that can be "doped" onto a surface layer (a fraction of a mono-layer thick) is less than can be contained in the volume of the alumino silicates. Contact ionization sources also tend to have larger ratio of emitted neutrals to emitted ions than do alumino-silicate sources, which accounts for most of the depletion at typical source temperatures.

Because both alumino-silicate and contact ionization sources operate at a hot-plate temperature of about $k_B T_i \sim 0.1$ eV, they produce sources which are relatively charge state pure due to the large values of the second ionization potential of the alkali metals. Due to modest ion depletion rates, pulse durations can generally be as long as the driving circuit can maintain voltage.

Gas discharge plasma sources: Most high current-density gas-discharge ion sources rely on extraction from a stationary, high-density and high-temperature plasma, which is produced from a neutral gas by electron impact ionization. To produce the ions, energetic electrons in the discharge plasma must liberate bound electrons. The ionization processes depend on the collision rate. Consequently, the electron density and temperature should be sufficiently high for efficient ionization. Recent experiments on these sources have demonstrated current-densities more than 100 mA/cm^2 [5]. However, as later discussed in the Section on multi-beamlet sources, this extraction scheme suffers from the current-density and emittance trade

off. Charge exchange of the ions with the background gas in the extraction gap is also an issue.

The usual process to make high charge-state ions is to liberate successive bound electrons by by the electron impact ionization. The process can be characterized by the parameter $J_e\tau_i = en_e v_e \tau_i$, where J_e is the electron current-density and τ_i is the ion confinement time. The important parameters for the discharge plasma ion source are the electron temperature $k_B T_e$, electron density n_e, electron current-density J_e, and the ion confinement time τ_i. A large flux of high-energy electrons is needed to produce a dense plasma of highly-stripped ions.

Vacuum arc sources: Metallic plasmas produced with vacuum arc discharges are also candidates for high current-density ion beams [11, 18]. Highly ionized ions formed from a vaporized metal arc plasma are utilized as an ion source. The available current-density and stability depend on the behavior of the arc and the electrode configuration. Typically, only ions of one charge state are desired for acceleration. Because the vacuum arc plasma is intrinsically transient, control of the surface fluctuations and the ionization degree are critical issues. In order to suppress the fluctuation, a number of types of grid controlled ion sources have been developed [4].

ECR sources: Electron Cyclotron Resonance (ECR) sources are plasma sources which are in widespread use for the production of high charge-state ions [19]. The source plasma is produced without cathodes using RF driven ECR heating of an initially neutral gas. They are reliable and stable because they do not have any consumable components except the beam source. High charge-state ions are produced by the impact of energetic electrons with neutrals and ions within a "minimum-B" magnetic field configuration used to both stably confine the plasma and allow for cyclotron instability. To increase the rate of ionization, the electron temperature ($k_B T_e$) is typically driven from 1 to 10 keV. On the other hand, the ion temperature ($k_B T_i$) should be held as low as possible because higher ion temperature produces an extracted beam with higher intrinsic emittance (see Sect. 9.1.1). In ECR sources, due to selective heating of electrons, ions in the source plasma can be low temperature. Because the plasma frequency is a function of the cut-off plasma density, microwave sources with higher frequencies are needed to reach higher plasma density in ECR ion sources. Recently, techniques have been developed that allow use of solid materials as the beam source, which extend the performance to a wide range of heavy ions. However, the available current of massive ions from solid materials in ECR sources is order of $\sim$100 μA [20].

EBIS sources: Electron Beam Ion Sources (EBIS) can produce extremely high charge-state ions. The EBIS device uses a nearly monoenergetic electron beam to bombard a neutral gas and produce highly-charged ions by electron impact ionization [21]. The electron beam only passes through the gas usually one time in a high vacuum. An electrostatic ion trap then stores ions produced with the desired charge state which can then be injected in an accelerator.

EBISs have provided the highest charge-state ions of all types of ion sources. Even fully stripped bare uranium nuclei are expected to be possible. However, only pulses with $\sim 10^{11}$ particles are possible with present trap technology. The relatively

low intensity of ions and difficult engineering requirements in the EBIS device are disadvantages for high current-density ion sources. However, a highly efficient EBIS using axially oscillating electrons is promising to enhance the number of extractable charges [14, 22, 23].

Laser sources: Laser irradiation of materials can produce dense plasmas from which ions can be extracted and formed into a beam. Such laser produced plasma sources provide a possible solution for high current-density and/or high charge-state ion extraction as well as high power applications. The target material is ablated as a dense drifting plasma that allows ion extraction exceeding conventional current-density limits. Properties of the ablation plasma are a strong function of the laser power density as well as the target geometry and material properties. Simplicity of operation, small size, and the capability to produce a wide variety of ion species with low emittance are advantages of laser ion sources. However, laser ion sources are in a developmental phase and further research is required for practical, economical source technology with high charge state purity and low characteristic spreads in energy and angular diversion. A laser ion source which overcomes that Bohm limit by direct ion injection has been proposed [24, 25] and research is progressing on sources employing ultra-high intensity, short-pulse lasers to irradiate thin foils [26, 27].

Negative ion sources: Negative ions are important for high flux neutral beam injectors in magnetic fusion devices [28] and have possible induction accelerator applications. Recent studies indicate that negative ions would be a possible source for high current ion accelerators, including drivers for Heavy Ion Fusion (HIF) [29]. The use of negative ions in beam transport can mitigate electron-cloud effects of concern for positive ions in high perveance sections. The vacuum requirements for accelerating and transporting high energy negative ions are estimated to be essentially the same as for positive ions. The halogens with their large electron affinities appear to be the most attractive candidates for high current negative ion sources. If desired, the beams could be photodetached to neutrals. An experiment conducted at LBNL using chlorine in an RF-driven source obtained a negative chlorine current-density of 45 mA/cm^2 under the same plasma conditions that gave a 57 mA/cm^2 positive chlorine current [29].

9.1.3 Example Injectors

Several example ion injectors are briefly reviewed to illustrate both typical working systems and design approaches made to achieve high currents.

Simple hot-plate diode: An example of a hot-plate diode is shown in Fig. 9.4. The Pierce electrode, source, exit electrode, and insulating support structure are shown in the figure. The flat, alumino-silicate source is 2.54 cm diameter and a 300 keV, 26 mA (apertured), long-pulse K^+ beam is extracted. The source is heated to ~0.1 eV and the $a = 10$ mm radius (apertured) extracted beam has measured emittance $\varepsilon_x = 14.2$ mm-mrad, which is a factor of 1.7 times higher than calculated

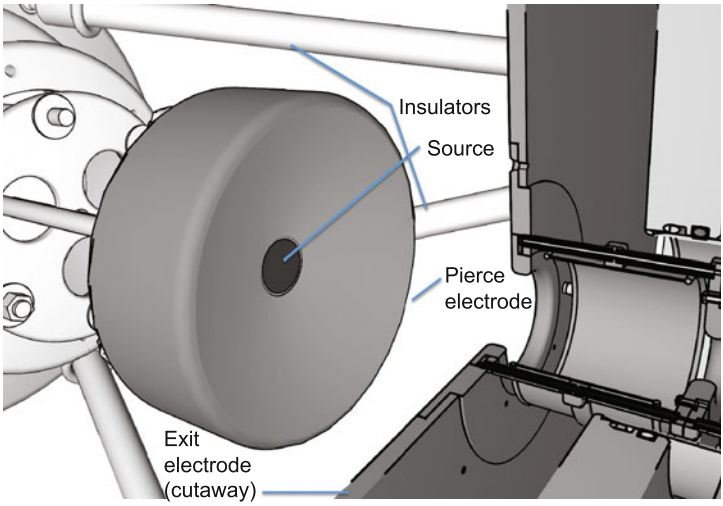

Fig. 9.4 A mechanical drawing of a hot-plate diode used on the NDCX-1 experiment at LBNL. One quarter of the exit electrode is cut away for viewing the source geometry (drawing courtesy M. Leitner, LBNL, 2010)

using Eq. (9.10) with $T_i = 0.1$ eV. Such emittance growth factors above simple ideal estimates are typical for hot-plate sources and are thought to result from nonlinear fields produced from both space-charge effects and the diode geometry.

Multi-beamlet sources: A possibility of overcoming the current-density limit with low beam emittance is to use multiple sources. Multiple-beam systems are well developed for neutral particle injectors and ion propulsion devices [30]. As can be seen from Eq. (9.9), the normalized emittance ε_{nx} is proportional to $T_i^{1/2}$. The beam brightness B is proportional to $I/\varepsilon_{nx}^2 \sim J_z/T_i$. But from the Child-Langmuir Law (Eq. 9.14) $J_z \sim V^{3/2}/d^2$; combined with the voltage breakdown law ($V \sim d^{1.0 \text{ to } 0.5}$), implies that the current-density scales as $J_z \sim V^{-1/2 \text{ to } -5/2} \sim d^{-1/2 \text{ to } -5/4}$ (cf. Eq. 9.7). Thus, small sources give high current-density, and so high beam brightness. The total beam current I, on the other hand is proportional to $\pi a^2 J_z$, and since maintaining good beam optics requires keeping $d/a >$ a constant (~ 4), $I \sim J_z d^2 \sim V^{3/2}$. So large current scales with large voltage and large sources. Applications that require both high brightness and high current are faced with a compromise. One way around the contradictory limitations, is by employing a multiple "beamlet" design where each small beamlet has high brightness, and then combining many beamlets into a single high current beam.

In low-energy, space-charge-dominated sections, high current-density miniature beamlets are contained in pre-accelerator grids. After the pre-acceleration, the beamlets are merged together to form a single beam composed of multiple beamlets. Independent control of individual beamlets allows steering for beam merging and focusing adjustments for envelope matching to be fulfilled simultaneously alleviating the need for usual matching sections between the source and transport lattice.

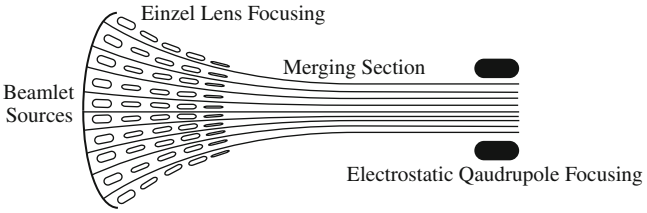

Fig. 9.5 Ion injector with multiple ion source beamlets

A multi-beamlet injector has been developed where 119, 2.2 mm diameter miniature Ar^+ beamlets with ~100 mA/cm^2 current-density are merged to single 70 mA, 400 keV beam with emittance $\varepsilon_x = 250$ mm-mrad [5, 31, 32]. A schematic of this injector is shown in Fig. 9.5. Simulations and experiment show that emittance growth is dominated by nonlinear space-charge effects in the merging process rather than the initial ion temperature, but that final emittance can be modest [33, 32].

Direct ion extraction from drifting plasma: One potential path towards increasing the ion current-density without increased emittance is to use a drifting plasma as an ion source. In case of plasma injection, the extractable current from a moving plasma is

$$J_i = q n_i v_d, \tag{9.19}$$

where v_d s the drift velocity of the source plasma [34]. The source plasma can be an electro-magnetically accelerated plasma or a laser ablation plasma. Based on this concept, drifting and point-expanding plasma sources have been proposed for high current ion injectors [35].

However, in the case of direct ion extraction from a drifting plasma, shape and position of the ion emitting surface is difficult to control. Behavior of the emitting surface is determined by the balance between the current produced by the plasma and the ability to extract ions in the effective acceleration gap. Figure 9.6 shows an illustration of the behavior of the space-charge potential of the direct injection gap. Although the dynamics driven by highly transient source plasma is still under investigation, it has been demonstrated that a high current-density, charge selected, and low emittance ion beam is possible to extract from a laser ablated expanding plasma [36, 37]. Experimental results show that the matching problem in which the plasma meniscus change is overcome when the operating condition is controlled to supply ions close to the space-charge limited current of the effective gap. At this matching condition, the plasma flux equals the effective space-charge limited value, and the emission surface becomes stationary. Using this configuration, a copper beam with $J_z = 100$ mA/cm^2 was produced with emittance $\varepsilon = 0.25$ mm-mrad, and flattop pulse duration 500 ns [24].

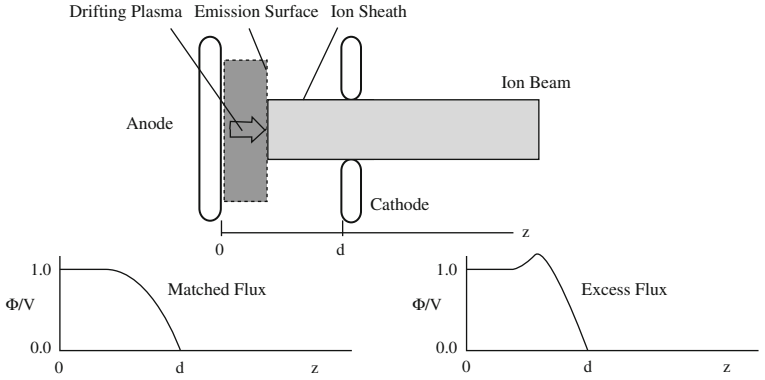

Fig. 9.6 Schematic of high current-density ion extraction from a drifting plasma

9.2 Longitudinal Beam Dynamics

One of the most significant differences between the physics of RF-accelerators and induction accelerators is the longitudinal dynamics resulting from the two different pulse formats. RF-accelerators generally form "micropulses" resulting from electric fields harmonically varying in time with frequency in the 100 MHz to several GHz range (corresponding to micropulses spanning ∼0.1 wavelength, of order 0.1–1.0 ns). Macro pulses are formed by strings of micropulses. Induction accelerators have no micro-pulses; instead macro-pulses in the ∼20 ns to ∼10 μs range are formed, which typically do not vary in current or energy during the "flattop" part of the pulse, and have ends which are confined by the application of electrical fields (sometimes called "ear" fields) which provide extra acceleration at the trailing end ("tail") of the pulse and some deceleration (relative to the flattop) at the leading end ("head") of the pulse. Since the beam length is typically large relative to the radius, analysis is often carried out using a "g-factor" approximation to the longitudinal electric field, to be discussed below.

The most complete solution to the coupled particle and field equations for the ions in a beam is obtained through numerical simulation. It is noted that 3D particle-in-cell methods, as well as direct Vlasov equation integrators have been used to describe both the longitudinal and transverse beam behavior most accurately. However, their details are not discussed here, because they are beyond the scope of the book.

9.2.1 Fluid Equation Approach

It is useful (for both a basic understanding of the beam physics and for accelerator design) to characterize the parallel beam dynamics using a reduced set of equations from the full Vlasov-Maxwell set. When the Vlasov equation is averaged over the

transverse coordinates and over the longitudinal velocity, a set of longitudinal fluid equations may be obtained. Since ion beam dynamics in induction accelerators is typically non-relativistic, for simplicity we use a non-relativistic formulation:

$$\frac{\partial \lambda}{\partial t} + \frac{\partial \lambda v}{\partial z} = 0 \tag{9.20}$$

$$\frac{\partial v}{\partial t} + v\frac{\partial v}{\partial z} = \frac{q}{m}E_z \tag{9.21}$$

Here, z is the longitudinal coordinate, t is time, $\lambda \equiv \int \rho \mathrm{d}x\mathrm{d}y$ is the line charge density, ρ is the charge density, v is the average longitudinal fluid velocity, and E_z is the longitudinal electric field (the sum of the space charge and externally applied field) averaged over the transverse coordinates. In Eq. (9.21), an additional term ($= -\frac{q\pi a^2}{m\lambda}\frac{\partial p}{\partial z}$ where p is the one dimensional pressure averaged over the beam radius a) has been dropped, because it is generally much smaller than the space charge term. To close the equations, a relationship between the electric field arising from space charge and the distribution of charge must be found.

9.2.2 "g-Factor" Descriptions of E_z

For an axisymmetric beam and infinite in longitudinal extent, Poisson's equation can be solved elementarily:

$$E_r = \frac{\lambda(r)}{2\pi\epsilon_0 r} \tag{9.22}$$

Here r is the radial coordinate, and $\lambda(r)$ denotes the line charge within radius r [and λ without an argument denotes $\lambda(r \to \infty)$]. When variations in r are much more rapid than variations in z then

$$\frac{\partial^2 \phi}{\partial z^2} \ll \frac{1}{r}\left(\frac{\partial}{\partial r} r \frac{\partial \phi}{\partial r}\right) \tag{9.23}$$

and we may calculate the beam potential by integrating radially from the pipe radius (where $\phi = 0$) to the radius r. If the charge density ($\rho = \rho_0$) is constant within the beam ($r < a$) and $\rho = 0$ outside of the beam ($r > a$) then the potential can be written:

$$\phi = \int \frac{\partial \phi}{\partial r}\mathrm{d}r = \begin{cases} \frac{\lambda}{2\pi\epsilon_0}\left[\frac{1}{2}\left(1 - \frac{r^2}{a^2}\right) + \ln\frac{b}{a}\right] & 0 < r < a \\ \frac{\lambda}{2\pi\epsilon_0}\ln\frac{b}{r} & a < r < b \end{cases} \tag{9.24}$$

Now, $E_z = -\partial\phi/\partial z$ may be calculated:

$$\frac{\partial \phi}{\partial z} = \frac{1}{2\pi\epsilon_0}\left[\frac{1}{2}\left(1 - \frac{r^2}{a^2}\right) + \ln\frac{b}{a}\right]\frac{\partial \lambda}{\partial z} - \frac{1}{2\pi\epsilon_0}\left[1 - \frac{r^2}{a^2}\right]\left(\frac{\lambda}{a}\right)\frac{\partial a}{\partial z}. \tag{9.25}$$

If $\rho = \text{const}$, then $\lambda/a^2 = \text{const}$, and

$$\frac{\partial \lambda}{\partial z} = \frac{2\lambda}{a}\frac{\partial a}{\partial z}, \tag{9.26}$$

so that

$$\frac{\partial \phi}{\partial z} = \frac{1}{2\pi\epsilon_0}\left(\ln\frac{b}{a}\right)\frac{\partial \lambda}{\partial z}. \tag{9.27}$$

Thus,

$$E_z = \frac{-g}{4\pi\epsilon_0}\frac{\partial \lambda}{\partial z}, \tag{9.28}$$

where $g \equiv 2\ln(b/a)$. The assumption of $\rho = \text{const}$ is most closely satisfied for space-charge dominated beams. When the beam is emittance dominated, the beam radius is not determined by λ so $\partial a/\partial z \simeq 0$. In that case,

$$\left\langle \frac{\partial \phi}{\partial z} \right\rangle = \frac{1}{2\pi\epsilon_0}\left[\frac{1}{2}\left(1 - \left\langle \frac{r^2}{a^2} \right\rangle\right) + \ln\frac{b}{a}\right]\frac{\partial \lambda}{\partial z}. \tag{9.29}$$

Here, the $\langle \ldots \rangle$ denotes an average taken over the radial coordinate. For a circular beam that has uniform density with respect to radius, $\langle r^2/a^2 \rangle = 1/2$, so that for emittance dominated beams, $g = 2\ln(b/a) + 1/2$. For beams that are intermediate between space charge dominated or emittance dominated, or are not uniform over radius, numerical evaluation may be required to accurately calculate g.

Combining Eqs. (9.21) and (9.28) yields:

$$\frac{\partial v}{\partial t} + v\frac{\partial v}{\partial z} = \frac{-qg}{2\pi m\epsilon_0}\frac{\partial \lambda}{\partial z} \tag{9.30}$$

The fluid equations (9.20) and (9.30) may now be solved, since the electric fields are treated as a local function of the line charge density, and the equations form a closed set.

9.2.3 Rarefaction Waves

One application of the fluid equations derived in Sects. 9.2.1 and 9.2.2 is the analysis of the longitudinal beam evolution of an initially uniform beam at the head or tail of the beam, as the space charge self-field acts to cause the beam to expand. As a mathematical simplification [38, 39] we assume that the line charge density initially makes a step in z from its constant value λ_0 to zero at the position of the the beam

end, which we place at $z = 0$. (Here we take z to be measured in the beam frame.) Expanding Eqs. (9.20) and (9.30) yields:

$$\frac{\partial \lambda}{\partial t} + v\frac{\partial \lambda}{\partial z} + \lambda\frac{\partial v}{\partial z} = 0 \tag{9.31}$$

$$\frac{\partial v}{\partial t} + v\frac{\partial v}{\partial z} + \frac{qg}{2\pi m\epsilon_0}\frac{\partial \lambda}{\partial z} = 0 \tag{9.32}$$

It is convenient to define $\Lambda \equiv \lambda/\lambda_0$, $V \equiv v/c_s$ and $\zeta \equiv v_0 z/c_s$ and $s \equiv v_0 t$ where $c_s^2 \equiv qg\lambda_0/4\pi\epsilon_0 m$, and v_0 is the beam velocity. Then Eqs. (9.31) and (9.32) become:

$$\frac{\partial \Lambda}{\partial s} + V\frac{\partial \Lambda}{\partial \zeta} + \Lambda\frac{\partial V}{\partial \zeta} = 0 \tag{9.33}$$

$$\frac{\partial V}{\partial s} + V\frac{\partial V}{\partial \zeta} + \frac{\partial \Lambda}{\partial \zeta} = 0 \tag{9.34}$$

We may try a similarity solution in the variable $x \equiv \zeta/s = v_0 z/(c_s s) = z/(c_s t)$. Since $\partial x/\partial s = -x/s$, and $\partial x/\partial \zeta = x/\zeta$, so that $\partial \Lambda/\partial s = (x/s)d\Lambda/dx$, etc., then Eqs. (9.33) and (9.34) can be expressed as a matrix equation:

$$\begin{bmatrix} V - x & \Lambda \\ 1 & V - x \end{bmatrix} \begin{bmatrix} \frac{\partial \Lambda}{\partial x} \\ \frac{\partial V}{\partial x} \end{bmatrix} = 0. \tag{9.35}$$

The substitution of the similarity variable x was successful in changing the fluid equations (which are partial differential equations in two independent variables) into a set of ordinary differential equations (with one independent variable), which is much easier to solve. For a nontrivial solution to exist, the determinant of the matrix in Eq. (9.35) must vanish. This implies that

$$\Lambda = (V - x)^2. \tag{9.36}$$

Taking the derivative of Eq. (9.36), and combining with the lower equation in Eq. (9.35) yields the simple equation: $\mathrm{d}V/\mathrm{d}x = 2/3$. The general solution to (9.35) is then:

$$V = \frac{2}{3}x + C \tag{9.37}$$

$$\Lambda = \left(-\frac{1}{3}x + C\right)^2 \tag{9.38}$$

To evaluate the integration constant C, we make use of the boundary and initial conditions. If the initial beam is such that $\Lambda = 1$ for $z < 0$ and $\Lambda = 0$ for $z > 0$, it is apparent that for $t > 0$, the solution extends from position x_- to position x_+, where $x_- < 0$ and $x_+ > 0$. Since $\Lambda = 1$ at $x = x_-$, the solution requires $x_- = 3C - 3$.

Similarly, $\Lambda = 0$ at $x = x_+$, requires $x_+ = 3C - 3$. To establish the constant C, we note that mass at positive z, originated at $z < 0$, so that mass conservation requires $-x_- = \int_{x_-}^{x_+} \Lambda(x)\mathrm{d}x$. From this constraint, simple algebra shows that $C = 2/3$, implying $x_- = -1$ and $x_+ = 2$. So the complete solution is:

$$\Lambda = \begin{cases} 1 & x < -1 \\ (-\frac{x}{3} + \frac{2}{3})^2 & -1 < x < 2 \\ 0 & x > 2 \end{cases} \tag{9.39}$$

$$V = \begin{cases} 0 & x < -1 \\ \frac{2}{3}(x+1) & -1 < x < 2 \\ 0 & x > 2 \end{cases} \tag{9.40}$$

The solution is plotted in Fig. 9.7. One qualitative feature of the solution is the space charge driven expansion of the tip of the beam away from the beam interior at twice the space charge wave speed ($x = 2$), and a rarefaction wave propagating towards the beam interior at a speed equal to the space charge wave speed ($x = -1$).

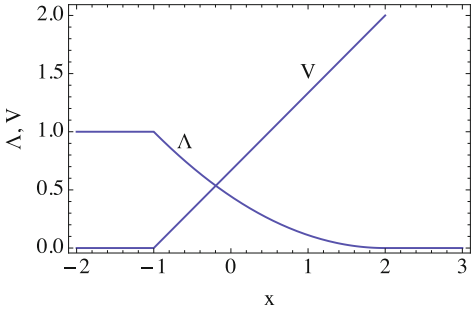

Fig. 9.7 Normalized line charge density Λ and velocity V in a self-similar space charge rarefaction wave, plotted against normalized position $x \equiv z/(c_s t)$

9.2.4 "Ear Fields"

As we have seen in Sect. 9.2.3, longitudinal space charge acts to increase the beam length. In order, to counteract the space charge, induction accelerators can employ externally imposed electric fields (so-called "ear fields," so named because the voltage profile resembles the floppy ears of a dog with one ear up and one ear down). These electric fields are also known as "barrier buckets."

For a beam with a line charge that is a constant over a length ℓ_{flat} but that falls off parabolically in the ends (each of length ℓ_{end}), the line charge can be written:

$$\lambda = \lambda_0 \begin{cases} 1 & |z| < \ell_{\mathrm{flat}}/2 \\ 1 - (|z| - \ell_{\mathrm{flat}}/2)^2/\ell_{\mathrm{end}}^2 & \ell_{\mathrm{flat}}/2 < |z| < \ell_{\mathrm{flat}}/2 + \ell_{\mathrm{end}} \\ 0 & \ell_{\mathrm{flat}}/2 + \ell_{\mathrm{end}} < |z| \end{cases} \tag{9.41}$$

Here z is the longitudinal coordinate measured in the beam frame, with beam center at $z = 0$. Use of Eqs. (9.41) and (9.28) results in an ear field equal to:

$$E_z = \frac{\text{sign}[z] g \lambda_0}{\pi \epsilon_0} \begin{cases} 0 & |z| < \ell_{\text{flat}}/2 \\ (|z| - \ell_{\text{flat}}/2)/\ell_{\text{end}}^2 & \ell_{\text{flat}}/2 < |z| < \ell_{\text{flat}}/2 + \ell_{\text{end}} \\ 0 & \ell_{\text{flat}}/2 + \ell_{\text{end}} < |z| \end{cases} \tag{9.42}$$

The maximum ear field for the line charge density (see Eq. 9.41) occurs at $|z| = \ell_{\text{flat}}/2 + \ell_{\text{end}}$ (i.e. the very tip of the beam) where it has value E_z (max) $= g\lambda_0/(\pi \epsilon_0 \ell_{\text{end}})$. Other models for the line charge density distribution, of course, will yield different results, but the value above is useful for order of magnitude estimates. As an example, for $\lambda_0 = 0.25\,\mu$C/m, $\ell_{\text{end}} = 0.3$ m, and $g = 1$, an electric field of 30 kV/m must be supplied to by the average accelerating gradient of the induction modules to keep the beam ends confined.

9.2.5 Longitudinal Waves

Just as pressure variations in a gas result in sound waves, line charge density fluctuations in a beam result in space charge waves. We may calculate some of the properties of space charge waves using the longitudinal fluid equations (9.20) and (9.21). For ease of calculation, we work in the beam frame, and we consider a long beam (ignoring the effects of the ends of the beam). We consider an equilibrium with uniform line charge density λ_0 and because we are working in the beam frame, zero equilibrium velocity ($v_0 = 0$). If we let $\lambda = \lambda_0 + \lambda_1$ and $v = v_0 + v_1$ and substitute into Eqs. (9.20) and (9.21), and linearize, we find:

$$\frac{\partial \lambda_1}{\partial t} + \lambda_0 \frac{\partial v_1}{\partial z} = 0 \tag{9.43}$$

$$\frac{\partial v_1}{\partial t} + \frac{c_s^2}{\lambda_0} \frac{\partial \lambda_1}{\partial z} = 0 \tag{9.44}$$

Here $c_s^2 \equiv q g \lambda_0/(4\pi \epsilon_0 m)$. Combining Eqs. (9.43) and (9.44) results in the familiar wave equation,

$$\frac{\partial^2 \lambda_1}{\partial t^2} - c_s^2 \frac{\partial^2 \lambda_1}{\partial z^2} = 0 \tag{9.45}$$

This has the well known general solution

$$\begin{aligned} \lambda_1 &= \lambda_0 \left(f_+[u_+] + f_-]u_-] \right), \\ v_1 &= c_s \left(-f_+[u_+] + f_-[u_-] \right). \end{aligned} \tag{9.46}$$

Here, $u_\pm = z \pm c_s t + C_0$, where C_0 is an arbitrary constant, and f_+ and f_- are arbitrary functions. From the solution, one can show that a pure density perturbation at $t = 0$ will decompose into a forward and backward going wave at later times. A sub class of solutions to Eq. (9.45) are harmonic solutions of the form $\lambda_1 = \tilde{\lambda_1} \exp[i\omega' t \pm ik'z]$. Here primes are a reminder that quantities are being calculated in the beam frame. Substitution into Eq. (9.45) yields the dispersion relation:

$$\omega' = \pm c_s k' \tag{9.47}$$

Thus the phase and group velocity of waves of all frequencies in the beam frame is c_s, the "space-charge wave" speed, which is consistent with the more general solution (9.46).

9.2.6 Longitudinal Instability

In the previous section, the equations assumed that image charge and currents did not change the longitudinal dynamics. However, image currents are impeded by the induction gaps, giving a high effective impedance. Further resistance in the pipe wall adds to the impedance although it usually gives a much smaller contribution to the impedance. Further, the gaps can act like capacitors which also changes the dynamics of the image current. We may model the physics of these interactions in the simplest case by placing a resistor and capacitor in parallel with a current source (equal to the image current). (See Fig. 9.8.) We may assume that a voltage ΔV is induced by the resistive and capacitive effects per induction module, each separated by a distance L. The image current is a current source, and must satisfy

$$I = C\frac{\mathrm{d}\Delta V}{\mathrm{d}t} + \frac{\Delta V}{R} \tag{9.48}$$

The average electric field $E = -\Delta V L$. Define $C^\dagger = CL$ and $R^* \equiv R/L$. Let $I = I_0 + I_1 \exp[-i\omega t]$ and $E = E_0 + E_1 \exp[-i\omega t]$ then linearizing Eq. (9.48) yields:

$$Z^* \equiv \frac{-E_1}{I_1} = \frac{R^*}{1 - i\omega C^\dagger R^*} \tag{9.49}$$

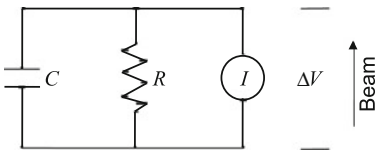

Fig. 9.8 Circuit representation of one module of many, each separated by a distance L

Now let's return to the 1D fluid equations. Let $\lambda = \lambda_0 + \lambda_1 \exp[-i(\omega t - kz)]$ and $v = v_0 + v_1 \exp[-i(\omega t - kz)]$ then linearizing Eqs. (9.20) and (9.21) *in the lab frame (in which $v_0 \neq 0$)* and using the generalized impedance $Z^*(\omega) \equiv -\frac{E_1}{I_1}$ and $I_1 = \lambda_0 v_1 + v_0 \lambda_1$ yields,

$$\begin{bmatrix} \omega - kv_0 & -k\lambda_0 \\ \frac{-c_s^2 k}{\lambda_0} + \frac{iqZ^*(\omega)v_0}{m} & \omega - kv_0 + \frac{iqZ^*(\omega)\lambda_0}{m} \end{bmatrix} \begin{bmatrix} \lambda_1 \\ v_1 \end{bmatrix} = 0 \tag{9.50}$$

The determinant of Eq. (9.50) must vanish for non-trivial solutions, which yields the dispersion relation:

$$(\omega - kv_0)^2 - c_s^2 k^2 + \frac{iqZ^*(\omega)\lambda_0 \omega}{m} = 0 \tag{9.51}$$

We may use a Galilean transformation to calculate the wave vector and frequency in the comoving beam frame ($\omega' = \omega - kv_0$ and $k' = k$, where prime indicates comoving frame variables). In terms of beam frame variables the dispersion relation, Eq. (9.51) can be expressed as:

$$\omega'^2 - c_s^2 k'^2 + \frac{iqZ^*(\omega', k')}{m} \lambda_0 (\omega' + k'v_0) = 0 \tag{9.52}$$

Here, $Z^*(\omega', k') \equiv Z^*(\omega = \omega' + k'v_0)$.

Let us now first examine the dispersion relation Eq. (9.52) when only resistance is present. Rearranging Eq. (9.52) gives,

$$\omega' = \pm c_s k' \sqrt{1 - \frac{iqR^*\lambda_0}{mc_s^2 k'^2}(\omega' + k'v_0)}. \tag{9.53}$$

Using the definition of c_s and assuming that the effects of the resistive term are small ($\omega'/k' \simeq c_s$), and that the space charge wave speed is much less than the ion beam velocity ($c_s \ll v_0$) yields

$$\begin{aligned} \omega' &= \pm c_s k' \sqrt{1 - \frac{i4\pi\epsilon_0 R^*}{g} \frac{v_0}{k'}} \\ &= \pm c_s k' \left(1 + \left(\frac{2\Gamma_R}{c_s k'}\right)^2\right)^{1/4} \times \left(\cos\left[\frac{1}{2}\tan^{-1}\left(\frac{2\Gamma_R}{c_s k'}\right)\right]\right. \\ &\quad \left. -i\sin\left[\frac{1}{2}\tan^{-1}\left(\frac{2\Gamma_R}{c_s k'}\right)\right]\right) \end{aligned} \tag{9.54}$$

$$\omega' \simeq \pm c_s k' \mp i\Gamma_R \qquad \text{for } 2\Gamma_R/(c_s k') << 1 \tag{9.55}$$

Here, $\Gamma_R \equiv 4\pi\epsilon_0 c_s v_0 R^*/(2g)$. Since the linearized quantities (such as λ_1 and E_1) were assumed to vary as $\exp[i(k'z - \omega' t)]$ choosing the upper sign in the dispersion relation Eq. (9.55), implies that $\omega' = c_s k'$ so that a line of constant phase $z = c_s t$, is forward propagating in the beam frame, and we find that the imaginary part of ω' is less than zero, which yields a decaying perturbation: $\lambda_1 \propto \exp[-\Gamma_R t]$. Similarly, choosing the lower sign in the dispersion relation (9.54) yields a backward propagating, growing wave. We define a logarithmic gain factor G by

$$G \equiv \Gamma_R t = \frac{4\pi\epsilon_0 c_s v_0 R^* t}{2g} \tag{9.56}$$

G is essentially the number of e-folds a backward propagating perturbation will grow in time t. The gain of a perturbation will be limited by the finite time in the accelerator (t_{res}) or the finite propagation time from head to tail (ℓ_b/c_s), where ℓ_b is the bunch length. If the former condition holds, G is proportional to $c_s \propto \lambda_0^{1/2}$ and so G is intensity dependent. However, if the latter condition holds $G \simeq 4\pi\epsilon_0 v_0^2 R^* \Delta t/(2g)$ where Δt is the pulse duration. Note that in this case G is independent of the current.

9.2.7 *Effects of Capacitance on Longitudinal Instability*

As discussed above, a more general lumped circuit model that describes the module impedance includes a capacitor in parallel with a resistor. The capacitance includes the "parallel plate" capacitance of the induction gap, and could include externally added capacitance to mitigate longitudinal instability. When Eq. (9.49) is inserted into Eq. (9.51) the lab frame dispersion relation becomes:

$$(\omega - k v_0)^2 - c_s^2 k^2 + \frac{iqZ^*(\omega)\lambda_0\omega}{m} = 0 \tag{9.57}$$

When capacitance is included in the lumped circuit the full Eq. (9.49) is needed. Separating the real and imaginary components of Eq. (9.49) yields:

$$Z^*(\omega) = \frac{R^*}{1 - i\omega C^\dagger R^*} = \frac{R^* + i\omega C^\dagger R^{*2}}{1 + \omega^2 C^{\dagger 2} R^{*2}} \tag{9.58}$$

Inserting Eq. (9.58) into Eq. (9.51) yields:

$$(\omega - k v_0)^2 - c_s^2 k^2 - \frac{q\omega^2 C^\dagger R^{*2}\lambda_0}{m(1 + \omega^2 C^{\dagger 2} R^{*2})} + \frac{iqR^*\lambda_0\omega}{m(1 + \omega^2 C^{\dagger 2} R^{*2})} = 0 \tag{9.59}$$

Expressed in terms of Γ_R and the space charge wave speed c_s, the dispersion relation becomes:

$$(\omega - kv_0)^2 - c_s^2 k^2 - \frac{2\Gamma_R (c_s/v_0)\omega^2 C^\dagger R^*}{(1+\omega^2 C^{\dagger 2} R^{*2})} + \frac{2\Gamma_R (c_s/v_0)\omega}{(1+\omega^2 C^{\dagger 2} R^{*2})} = 0 \tag{9.60}$$

Equation (9.60) can be expressed in the beam frame as:

$$\omega'^2 - c_s^2 k'^2 - \frac{2\Gamma_R (c_s/v_0)(\omega' + k'v_0)^2 C^\dagger R^*}{(1+(\omega' + k'v_0)^2 C^{\dagger 2} R^{*2})} + \frac{2\Gamma_R (c_s/v_0)(\omega' + k'v_0)}{(1+(\omega' + k'v_0)^2 C^{\dagger 2} R^{*2})} = 0 \tag{9.61}$$

It is clear, that if $C^\dagger$ is large, the second and third term can be reduced, thus reducing the instability growth rate. In particular, if $2(v_0/c_s)\Gamma_R R^* C^\dagger << 1$, then the third term in Eq. (9.61) will be much less than the second, so the real part of the dispersion relation will not be significantly changed, and thus $\omega' \simeq c_s k'$. In that case, the steps leading to Eq. (9.56) can be repeated leading to:

$$\begin{aligned}
\omega' &= \pm c_s k' \sqrt{1 - i\frac{2\Gamma_R}{c_s k' \left(1 + (k' v_0 R^* C^\dagger)^2\right)}} \\
&= \pm c_s k' \left(1 + \left(\frac{2\Gamma_R}{c_s k' \left(1 + (k' v_0 R^* C^\dagger)^2\right)}\right)^2\right)^{1/4} \\
&\quad \times \left(\cos\left[\frac{1}{2}\tan^{-1}\left(\frac{2\Gamma_R}{c_s k' \left(1 + (k' v_0 R^* C^\dagger)^2\right)}\right)\right]\right. \\
&\quad \left. -i \sin\left[\frac{1}{2}\tan^{-1}\left(\frac{2\Gamma_R}{c_s k' \left(1 + (k' v_0 R^* C^\dagger)^2\right)}\right)\right]\right)
\end{aligned} \tag{9.62}$$

$$\omega' \simeq \pm c_s k' \mp i\frac{\Gamma_R}{1 + (k' v_0 R^* C^\dagger)^2} \quad \text{for} \quad \frac{2\Gamma_R}{c_s k' (1 + (k' v_0 R^* C^\dagger)^2)} << 1 \tag{9.63}$$

The growth rate now depends on k' (at large k'). For a perturbation with k' less than $2\pi/l_b$ the perturbation wavelength would be longer than the beam length l_b, and so the perturbation is not likely to grow. So if $2\pi v_0 R^* C^\dagger / l_b > 1$, the second term in the denominator of the imaginary term of Eq. (9.63) will significantly reduce the growth rate.

Consider an example, from a proposed application discussed in Chap. 10, a high current heavy ion accelerator for inertial fusion. Typical designs might have beams with ion velocities $v_0 = 10^8$ m/s, current $I = 3$ kA, bunch length $l_b = 10$ m, $g = 1.8$, $R^* = 100\,\Omega$/m, yielding a resistive growth rate $\Gamma_R = 1.5 \times 10^5$ s^{-1}. The logarithmic gain G would be $\Gamma_R l_b / c_s = 3$ if the growth time were limited by head to tail growth, or $\Gamma_R l_{\text{acc}}/v_0 = 1.5$ if the growth time were limited by the

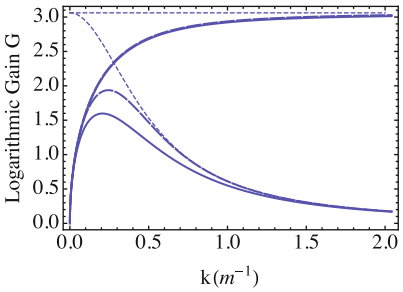

Fig. 9.9 Logarithmic Gain G of the longitudinal instability as a function of perturbation wavenumber k, for $R^* = 100\,\Omega/\text{m}$, $C^\dagger = 0$ (*upper curves*) and $C^\dagger = 2 \times 10^{-10}$ F-m (*lower curves*), after a growth time corresponding to l_b/c_s, where $l_b = 10$ m and $c_s = 4.9 \times 10^5$ m, calculated from numerical solution (*solid curves*) to Eq. (9.51), analytic solutions from Eqs. (9.54) and (9.62) (*long dashed curves*) and asymptotic expressions from Eqs. (9.55) and (9.63) (*short dashed curves*). Other parameters are given in the text

length of the accelerator l_{acc}, here assumed to be 10^3 m. If $C^\dagger = 5 \times 10^{-12}$ F-m the growth, there would be a measurable reduction in growth. Simulations [40] using above parameters with 40 times larger capacitance, show essentially no growth of a perturbation. Figure 9.9 shows the the logarithmic gain obtained from the exact numerical solution of Eq. (9.51), using the parameters above, together with the analytic solutions discussed above.

The above calculations may be repeated with finite inductance in the circuit equation. The lesson to draw is that for high current applications, beam interactions with the structure of the accelerator need to be assessed and, if necessary, addressed. This low frequency longitudinal resistive instability is only one example of beam/accelerator interactions. See Chap. 7 for an example of a high frequency transverse beam/accelerator interaction known as the beam-break-up instability (or BBU).

9.3 Transverse Dynamics Issues

As mentioned in Introduction, the physics of transverse ion dynamics in induction linacs has been not covered here. Beam dynamics in the non-relativistic and space-charge dominated regime, which characterizes ions in induction linac, has been extensively developed for RF linacs as well as induction linacs. A lot of articles are available in Journal papers [41] and related topics have been given as lectures at the established US particle accelerator schools [42]. In addition, there are crucial and practical issues to design a beam transport line and analyze the behavior of ion beam there. They are listed below.

1. Beam envelope mismatching originating from perturbations in the lattice parameters or beam loss through the beam line [42].
2. Coupling effects between transverse and longitudinal motions arising in longitudinal beam manipulations [43–45].

3. Beam halo driven by nonlinear space-charge effects or beam core breathing [46].
4. Two stream instability caused by the coherent interaction with electron clouds emitted from the surrounding surface or created as a result of ionization of residual gas atoms [47].
5. Transverse instability (BBU) caused by wake fields in the surrounding devices [4].

Readers who are interested in these subjects are advised to refer to the related articles shown above, and they should also be able to get useful information from the recent proceedings of accelerator conferences such as PAC, EPAC, APAC, and IPAC.

References

1. M. Reiser. *Theory and Design of Charged Particle Beams*, Wiley, New York, NY, 1994.
2. R. Miller. *An Introduction to the Physics of Intense Charged Particle Beams*, Plenum Press, New York, NY, 1982.
3. A. Chao and M. Tigner, editors. *Handbook of Accelerator Physics and Engineering*, World Scientific, New York, NY, 1999. A. Faltens, p. 475.
4. S. Humphries. *Charged Particle Beams*, Wiley, New York, NY, 1993.
5. J. Kwan. High Current Ion Sources and Injectors for Induction Linacs in Heavy Ion Fusion. *IEEE Trans. Plasma Sci.*, 33:1901, 2005.
6. E. Startsev, R. Davidson, and H. Qin. Anisotropy-Driven Collective Instability in Intense Charged Particle Beams. *Phys. Rev. Spec. Topics Accl. Beams*, 8:124201, 2005.
7. E. Startsev, R. Davidson, and H. Qin. Nonlinear δf Simulation Studies of Intense Charged Particle Beams with Large Temperature Anisotropy. *Phys. Plasmas*, 9:3138, 2002.
8. S. Lund, D. Callahan, A. Friedman, D. Grote, I. Haber, and T. Wang. Theory of an Electrostatic Instability Driven by Transverse-Longitudinal Temperature Anisotropy in Space Charge Dominated Beams. In *Proceedings of the 1998 Linear Accelerator Conference*, pages 372–376, TU2004, New York City, NY, August 23–28, 1998.
9. R. Davidson. *Physics of Nonneutral Plasmas*. Addison-Wesley, Reading, MA, 1990. Rereleased, World Scientific, Singapore, 2001.
10. R. Davidson. Electrostatic Shielding of a Test Charge in a Nonneutral Plasma. *J. Plasma Phys.*, 6:229, 1971.
11. I. Brown. *The Physics and Technology of Ion Sources*, Wiley, New York, NY, 1989.
12. A. Forrester. *Large Ion Beams: Fundamentals of Generation and Propagation*. Wiley-Interscience, New York, NY, 1988.
13. M. Lampel and M. Tiefenback, Appl. Phys. Lett. 43, 57 (1983).
14. R. Becker. Electron Beam Ion Sources and Traps. *Rev. Sci. Inst.*, 71:816, 2000.
15. J. Kwan, F. Bieniosek, E. Henestroza, L. Prost, and P. Seidl. A 1.8 MeV K+ Injector for the High Current Beam Transport Experiment. *Laser Part. Beams*, 20:441, 2002.
16. F. Bieniosek, C. Celata, E. Henestroza, J. Kwan, L. Prost, P. Seidl, A. Friedman, D. Grote, S. Lund, and I. Haber. 2-MV Electrostatic Quadrupole Injector for Heavy-Ion Fusion. *Phys. Rev. Spec. Topics Accel. Beams*, 8:010101, 2005.
17. L. Smith and R. Breitwieser. Richardson-Dushman Equation Monograph. *J. Appl. Phys.*, 41: 436–437, 1970.
18. H. Rutkowski, D. Hewett, and S. Humphries, Jr. Development of Arc Ion Sources for Heavy Ion Fusion. *IEEE Trans. Plasma Sci.*, 19:782, 1991.
19. V. Semenov, V. Skalyga, A. Smirnov, and V. Zorin. Scaling for ECR Sources of Multicharged Ions with Pumping at Frequencies from 10 to 100 GHz. *Rev. Sci. Inst.*, 73:635, 2002.

20. D. Wutte, S. Abbott, M.. Leitner, and C. Lyneis. High Intensity Metal Ion Beam Production with ECR Ion Sources at the Lawrence Berkeley Laboratory. *Rev. Sci. Inst.*, 73:521, 2002.
21. A. Kponou, E. Beebe, A. Pikin, G. Kuznetsov, M. Batazova, and M. Tinov. Simulation of 10 A Electron-Beam Formation and Collision for a High Current Electron-Beam Ion Source. *Rev. Sci. Inst.*, 69:1120, 1998.
22. R. E. Marrs. *Experimental Methods in the Physical Sciences 29A: ATOMIC, MOLECULAR, AND OPTICAL PHYSICS: CHARGED PARTICLES*. Academic Press, San Diego, CA, 1995.
23. J. Sun, N. Nakamura, M. Tona, C. Yamada, H. Watanabe, S. Ohtani, and Y. Fu. Growth of Ionization Balance from F-like to Bare Ions of Heavy Atoms in an Electron Beam Ion Trap. *Plasma Fusion Res.*, 3:052, 2008.
24. M. Nakajima, N. Kobayashi, K. Horioka, J. Hasegawa, and M. Ogawa. Direct Extraction of Ions from Expanding Laser Ablation Plasma. Technical Report Reserach Report NIFS-PROC-61, page 149, National Institute for Fusion Science, Toki, Japan, 2005.
25. M. Okamura, T. Katayama, R. Jameson, T. Takeuchi, T. Hattori, and H. Kashiwagi. Scheme for Direct Plasma Injection into an RFQ Linac. *Laser Part. Beams*, 20:451, 2002.
26. A. Henig, S. Steinke, M. Schnürer, T. Sokollik, R. Hörlein, D. Kiefer, D. Jung, J. Schreiber, B. Hegelich, X. Yan, J. Meyer ter Vehn, T. Tajima, P. Nickles, W. Sandner, and D. Habsy. Radiation-Pressure Acceleration of Ion Beams Driven by Circularly Polarized Laser Pulses. *Phys. Rev. Lett.*, 103:245003, 2009.
27. B. Hegelich, B. Albright, J. Cobble, K. Flippo, S. Letzring, M. Paffett, H. Ruhl, J. Schreiber, R. Schulze, and J. Fernández. Laser Acceleration of Quasi-Monoenergetic MeV Ion Beams. *Nature*, 439:441–444, 2006.
28. W. Cooper. Neutral Beam Injectors for the International Thermonuclear Experimental Reactor. *Phys. Fluids B*, 4:2300, 1992.
29. L. Grisham, S. Hahto, S. Hahto, J. Kwan, and K. Leung. Experimental Evaluation of a Negative-Ion Source for a Heavy-Ion Fusion Negative-Ion Driver. *Nucl. Inst. Meth. A*, 544: 216, 2005.
30. Y. Hayakawa and S. Kitamura. Ion Beamlet Divergence Characteristics of Two-Grid Multiple-Hole Ion Thruster. *J. Propulsion Power*, 15:377–382, 1999.
31. J. Kwan, F. M. Bieniose, D. P. Grote, and G.A. Westenskow. Compact Multibeamlet High-Current Injector for Heavy-Ion Fusion Drivers. *Rev. Sci. Inst.*, 77:03B503, 2006.
32. G. Westenskow, J. Kwan, D. Grote, and F. Bieniosek. High-Brightness Heavy-Ion Injector Experiments. *Nucl. Inst. Meth. A*, 577:168–172, 2007.
33. D. Grote, E. Henestroza, and J. Kwan. Design and Simulation of a Multibeamlet Injector for a High Current Accelerator. *Phys. Rev. Spec. Topics Accel. Beams*, 6:014202, 2003.
34. M. Dembinski, P. K. John, and A. G. Ponomarenko. High-Current Ion Beam from a Moving Plasma. *Appl. Phys. Lett.*, 34:553, 1979.
35. K. Horioka, J. Hasegawa, M. Nakajima, H. Iwasaki, H. Nakai, K. Hatsune, M. Ogawa, K. Takayama, J. Kishiro, M. Shiho, and S. Kawasaki. Long-Pulse Ion Induction Linac. *Nucl. Inst. Meth. A*, 415:291, 1998.
36. M. Yoshida, J. Hasegawa, J. Kwan, Y. Oguri, K. Horioka, and M. Ogawa. Grid-Controlled Extraction of Low-Charged Ions from a Laser Ion Source. *Japanese J. Appl. Phys.*, 42:5367, 2003.
37. M. Ogawa, M. Yoshida, M. Nakajima, J. Hasegawa, S. Fukuda, K. Horioka, and Y. Oguri. High-Current Laser Ion Source Based on a Low-Power Laser. *Laser Part. Beams*, 21:633, 2004.
38. L. Landau and L. Lifshitz. *Fluid Mechanics*, Pergamon Press, Elmsford, New York, NY, 1987.
39. A. Faltens, E. Lee, and S. Rosenblum. Beam End Erosion. *J. Appl. Phys.*, 61:5219, 1987.
40. D. Callahan. *Simulations of Longitudinal Beam Dynamics of Space-Charge Dominated Beams for Heavy Ion Fusion*. PhD thesis, University of California at Davis, 1994.
41. S. Lund and B. Bukh. Stability Properties of the Transverse Envelope Equations Describing Intense Ion Beam Transport. *Phys. Rev. Spec. Topics Accel. Beams*, 7:024801, 2004.

42. J. Barnard and S. Lund. U.S. Particle Accelerator School Courses. *Beam Physics with Intense Space-Charge*, Annapolis, MD, 16–27 June 2008, Lawrence Livermore National Laboratory, LLNL-AR-407617 and Lawrence Berkeley National Laboratory, LBNL-1097E; *Beam Physics with Intense Space-Charge*, Waltham, MA, 12–23 June 2006, Lawrence Livermore National Laboratory, UCRL-TM-231628 and Lawrence Berkeley National Laboratory, LBNL-62783; *Intense Beam Physics: Space-Charge, Halo, and Related Topics*, Williamsburg, VA, 19–20 January, 2004, Lawrence Livermore National Laboratory, UCRL-TM-203655 and Lawrence Berkeley National Laboratory, LBNL-54926; *Space-Charge Effects in Beam Transport*, Boulder, CO, 4–8 June, 2001, Lawrence Berkeley National Laboratory, LBNL-49286. Course notes are also archived on the US Particle Accelerator School web site: http://uspas.fnal.gov/
43. H. Okamoto and H. Tanaka. Proposed Experiments for the Study of Beam Halo Formation. *Nucl. Inst. Meth.*, A-437:178, 1999.
44. T. Kikuchi and K. Horioka. Beam Behavior Under a Non-stationary State in High-Current Heavy Ion Beams. *Nucl. Inst. Meth.*, A-606:31, 2009.
45. L. Groening, I. Hoffmann, W. Barth, W. Bayer, G. Clemente, L. Dahl, P. Forck, P. Gerhard, M. S. Kaiser, M. Maier, S. Mickat, T. Milosic, and S. Yaramyshev. Experimental Evidence of Space Charge Driven Emittance Coupling in High Intensity Linear Accelerators. *Phys. Rev. Lett.*, 103:224801, 2009.
46. J. Wei, W. Fisher, and P. Manning, editors. *Beam Halo Dynamics, Diagnostics, and Collimation, AIP Conference Proceedings No. 693*. The American Institute of Physics, Woodbury, New York, NY, 2003.
47. A. Molvik, Experiments and Simulations of Electrons in a Linac with 4 μs Duration Ion Beam, (Electron Cloud Feedback Workshop, March 13–15, 2007), available at http://physics.indiana.edu/~shylee/ap/mwapc/epws.html